Electro-mechanical Simulation of a Large Aperture MOEMS Fabry-Perot Tunable Filter

Jonathan L. Kuhn, Richard B. Barclay, Matthew A. Greenhouse,
D. Brent Mott, Shobita Satyapal

NASA/Goddard Space Flight Center, Greenbelt, MD 20771

ABSTRACT

We are developing a micro-machined electrostatically actuated Fabry-Perot tunable filter with a large clear aperture for application in high through-put wide-field imaging spectroscopy and lidar systems. In the first phase of this effort, we are developing key components based on coupled electro-mechanical simulations. In particular, the movable etalon plate design leverages high coating stresses to yield a flat surface in drum-head tension over a large diameter (12.5 mm). In this approach, the cylindrical silicon movable plate is back etched, resulting in an optically coated membrane that is suspended from a thick silicon support ring. Understanding the interaction between the support ring, suspended membrane, and coating is critical to developing surfaces that are flat to within stringent etalon requirements. In this work, we present the simulations used to develop the movable plate, spring suspension system, and electrostatic actuation mechanism. We also present results from tests of fabricated proof of concept components.

Keywords: simulation, electro-mechanical, Fabry-Perot, tunable filter, membrane, optical coating

1. INTRODUCTION

A conventional Fabry-Perot (FP) interferometer or etalon consists of two flat, parallel, semi-transparent plates coated with films of high reflectivity and low absorption. The pass band of the etalon is determined by the separation between the plates, which is generally varied using piezoelectric translators (PZT). Fabry-Perots have been used extensively for the last several decades over a wide range of wavelengths. Queensgate Instruments,[1] for example, have provided a number of scientifically fruitful state of the art Fabry-Perots. However, these etalons have been traditionally operated at room temperature and at moderate to high resolving powers ($R > 500$). Options for low resolution variable interference filters have typically been restricted to circular variable filters or linear variable filters. These options require an optical design that includes a small (1-2 mm diameter) pupil. With the advent of large aperture wide field telescopes, incorporating a small pupil in the optics design while retaining good image quality and spectral purity over the desired field of view (FOV) is extremely difficult. Such a situation will exist in any camera design for the Next Generation Space Telescope (NGST).[2] In such situations, low resolution FPs are an ideal option for narrow-band imaging. They ease size requirements on filter wheels and offer flexibility in the choice of spectral resolution. However, no such cryogenic low order tunable filter existed prior to the development at NASA/GSFC of a Demonstration Unit for Low-order Cryogenic Etalon, (DULCE).[3] DULCE has been very successful, however still uses bulky plates and 'macro' machining techniques. In this effort, we are developing a micro-electromechanical systems (MEMS) FP that offers several advantages for cryogenic space flight applications.

Modern conventional large aperture Fabry-Perots typically utilize thick massive mirrors to achieve flatness, piezo electric translators (PZT) as mechanical actuators, and capacitance micrometers as position transducers. When conventional Fabry-Perots are used in high G flight applications and other field applications involving vibration and shock loads, the massive etalon plates impart high shear loads on the actuators resulting in damage. Typical infrared applications require cooling the Fabry-Perot to cryogenic temperatures. PZTs offer very limited stroke at these temperatures and magneto-strictive actuators do not enable room temperature testing. Conventional Fabry-Perots are delicate, expensive, bulky, hand assembled units. All of these difficulties in applying conventional Fabry-Perot technology to space flight instruments are eliminated by the MEMS design presented herein.

In the large aperture MEMS design, the entire etalon assembly is produced by micro-machining. The massive mirrors of conventional etalons are replaced by thin ($\sim 10\ \mu m$) high flatness films such that inertial forces acting on the mirrors are negligible. As a consequence, vibration induced inertial loads are eliminated and very low actuator

E-mail correspondence: Jonathan.Kuhn@gsfc.nasa.gov

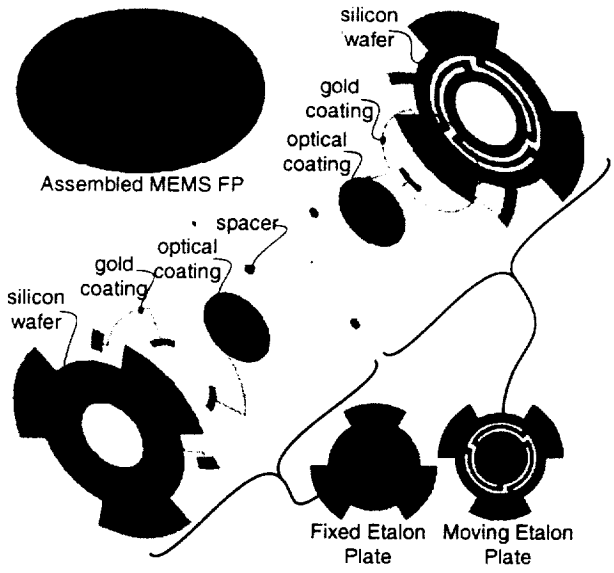

Figure 1. Solid model rendering of the MEMS FP concept.

force levels are required to achieve high frequency response. Simple capacitive electrostatic actuators can be used yielding near zero power dissipation. The resulting Fabry-Perot assembly functions at both room and cryogenic temperatures. This MEMS approach offers low thermal mass for rapid cooling and a compact package similar to a standard interference filter. Hand assembly of numerous complex parts is eliminated and replaced by a monolithic MEMS part yielding low unit cost. The resulting superior functionality, compact package, and low cost will make advanced tunable filter capability available to small low cost flight instruments for the first time.

In this paper, we present the details of the design and electro-mechanical simulation of the large aperture MEMS Fabry-Perot. In this stage of the work, the device development is subdivided into two key technologies, which are the multi-layer dielectric reflector membranes and the servo mechanism. Design and analysis of each of these components are presented, and fabrication and testing are outlined. Preliminary results from coating tests are also presented.

2. DESIGN CONCEPT

Fig. 1 shows a solid model of the 12.5 *mm* aperture MEMS Fabry-Perot design concept. The assembled FP is shown in the upper left, and a corresponding exploded view is shown in the center. The lower right of the above figure also shows plan views of both the upper (movable) etalon plate, and lower (fixed) etalon plate. The exploded view of the mechanism illustrates the various layers also shown in Fig. 2.

In this design, the mechanism is fabricated in two sections that are assembled into the final product. The base section consists of a 400 μm silicon wafer, which is coated with a multi-layer dielectric (MLD) in the aperture, and has metallized pads for electrostatic actuation and sensing. These are connected via metal traces to bond pads for external connection. The upper section consists of a 400 μm silicon layer, which is also coated with MLD over the aperture. The upper reflector is suspended from an outer annulus by silicon leaf springs to allow articulation of the upper reflector. The upper section also has metallized pads spaced along an annulus around the aperture for actuation and sensing, which are connected via radial traces to bond pads on the outer, stationary annulus. The two sections are epoxied together with spacers between them along the outer annulus.

Plate flatness is critical to achieving science grade performance in a Fabry-Perot filter. In our design, the two etalon plates consist of thin silicon nitride membranes with dielectric coatings. The pre-stressed coating materials (e.g. IRX200 and Silicon multi-layers) will yield flat films in net drum-head tension. We have chosen fabrication techniques outlined below that yield a round part to eliminate stress concentration in the etalon plates.

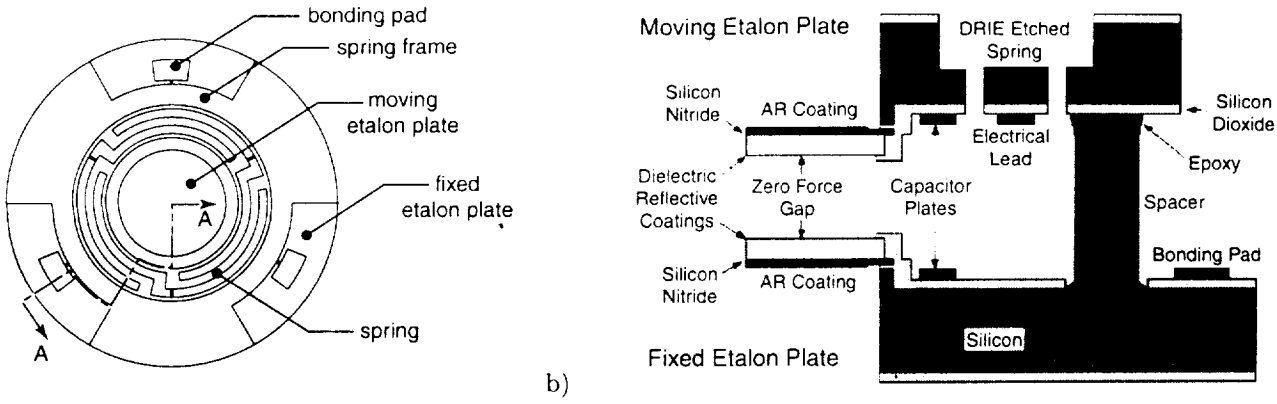

Figure 2. a) Top view of the assembled MEMS FP. b) Schematic cross section view showing the fabricated layers (not to scale).

The moving plate is suspended on three leaf springs. The spring assembly is designed to allow scanning of the Fabry-Perot gap and provides rotational freedom for parallelism adjustment. Three gold capacitance pads are deposited onto the moving and fixed plates. A DC (~ 35 V) bias across these pads generates an attractive force that works against the restoring force of the spring. These actuators are controlled individually for parallelism adjustment and in unison for gap adjustment. An AC (~10 kHz) bias across the same capacitance pads will be demodulated to provide sensing feedback. This configuration allows each actuator to be operated as a position servo under computer control. The pad size and actuator gap are designed to allow sufficient throw with a reasonable amount of voltage and margin to avoid "snap on" and stiction.

The suspension springs are sized along with the actuators to provide sufficient force to hold the membrane, yet be compliant enough to allow actuation. The electrostatic actuators only provide an attractive force. Therefore, the springs provide the restoring force required to move the reflectors apart. To ensure controllability, the etalon plates are assembled with a larger gap than required for operation and a bias voltage applied to bring the gap within operational range.

The control system builds on the DULCE work, which has the same requirements for gap spacing and parallelism and uses similar parallel-plate capacitive sensors. The actuator driver and control algorithm is modified. Presently, DULCE uses piezo electric actuators. The attractive force of the electrostatic actuators is nonlinear with distance, which presents a somewhat more complicated control problem. Digital control algorithms will be implemented with an off-the-shelf Digital Signal Processor (DSP) based controller. Because flight hardware implementation solutions exist, effort can be focussed on developing the control algorithm.

The end-product will be very compact and robust and will easily be accommodated into the NGST Near Infrared Camera. For instance, one of several MEMS FPs, each covering a different wavelength region, could be inserted into either a wheel or a simple insertion/removal mechanism.

2.1. Fabrication Process

The fabrication process makes extensive use of Deep Reactive Ion Etching (DRIE) of silicon. DRIE allows the etching of arbitrary shapes vertically into a silicon wafer without the crystal plane dependence of wet chemical anisotropic etches. The thick curved springs and circular aperture are natural applications for this technology.

The process for the top moving etalon structure begins with a 100 *mm* diameter silicon wafer. The wafer is coated on both sides by Low Pressure Chemical Vapor Deposition (LPCVD), first with a silicon dioxide film and then with silicon nitride. The silicon dioxide will later act as an effective etch stop for the DRIE and the silicon nitride as mechanical support and protection for the dielectric coating. The dielectric coating is deposited through a shadow mask to form a disk in the center of the top of the wafer with a diameter larger than the clear aperture.

The exposed silicon is then etched down so that the dielectric is left on a raised mesa. This step in the surface is intended to create different gap dimensions for the etalons and the actuation capacitance plates. The exposed

silicon is again coated with silicon dioxide to act as an electrical insulator. Gold is deposited on top of the oxide and patterned to form the capacitor actuation and reference plates, electrical leads, and wire bonding pads. From the front side, the silicon is etched by DRIE in the shape of springs to a depth equal to the desired spring thickness.

The next steps involve etching on the back side of the wafer. Because the wafer will be etched completely through in some places, the wafer is mounted face down to a 100 *mm* quartz wafer with a low temperature wax. The transparent wax and quartz allows precise optical alignment of features on the front and back of the wafer. In a series of DRIE steps, the wafer is etched from the back to release the springs, remove the silicon in the free aperture behind the dielectric coating, and delineate the outside edge of the device. The silicon dioxide on the front surface of the silicon etches much slower than the silicon removed with hydrofluoric acid, which does not etch silicon or silicon nitride. This process leaves the silicon nitride film behind the dielectric for support and protection. The anti-reflection (AR) coatings can then be deposited through a shadow mask onto the silicon nitride in the aperture.

The wafer is subsequently placed in a solvent bath and the wax dissolved away to release the moving etalon structure from the quartz wafer. The bottom fixed etalon structure is fabricated in a similar way except for a few differences. The fixed plate does not have the DRIE etched springs and there are recessed areas on its front side used to set the spacing between the etalon structures.

The top moving etalon structure is flipped over and epoxied face down to the bottom fixed etalon structure using a precision spacer to achieve the desired gap. The recessed regions in the bottom structure are used to modify the gap from the thickness of standard spacers. An edge of the completed device is shown if Fig. 2b. The dimensions of the thin films have been exaggerated for clarity.

Due to the complicated nature of the integrated device development, we choose to pursue two development paths. The first is that of the reflector coatings, and the second is that of the servo mechanism. Each of these paths are developed with subsequent integration in mind. Our immediate objective is to produce test components for each of these key technologies for proof of concept. In the following sections we present the details of the reflector and mechanism designs and simulations, along with preliminary test results and discussion of future testing.

3. REFLECTORS

In order to cover a broad-band, several layers of dielectric are generally deposited on a substrate optic. The materials chosen and thicknesses are designed not only to provide the desired optical performance, but also to be compatible with the rest of the micro-machining. Preliminary examination and consultation with vendors conclude that this can be achieved with focused developmental work, and it is the objective of this work to develop these coatings.

The coated optics must be flat to with 6 *nm*. Historically this requirement is complicated by the intrinsic stress within the coating materials. Typically, this issue is addressed by applying the coating to thick substrates whose stiffness is sufficient to keep the surface flat despite the coating stress. The MEMS design concept requires reflectors that are much thinner than is conventionally used. As a result we deposit the MLD coating on a silicon wafer and then etch away the wafer, leaving a thin membrane for the reflector. The coating extends beyond the clear aperture and overlaps an un-etched annular structure much like a drum-head. The coating stress tensions the membrane across the drum, pulling the membrane flat over the aperture. The following finite element model shows that this is theoretically possible. We are in the process of designing the stress required to produce the flatness without inducing failure.

3.1. Finite Element Analysis

Preliminary finite element analysis of a hypothetical membrane system has been completed as shown in Fig. 3. The model is comprised of a 400 μm thick silicon ring supporting a suspended membrane of low stress 0.5 μm thick silicon nitride coated with 10 μm of gold with an intrinsic stress of 100 MPa. A finite element model of an axi-symmetric slice of the system was developed to determine the flatness of such a membrane after back etching. In this case, the peak to valley offset in the region marked "flat" is approximately 0.006 μm. While hypothetical, this result indicates that a very high degree of flatness may be achieved with this configuration.

These results may be validated by etching circular holes into silicon wafers with silicon nitride coatings. We are currently in the process of completing these tests. However, the fabrication was not completed at the time of submission for this manuscript.

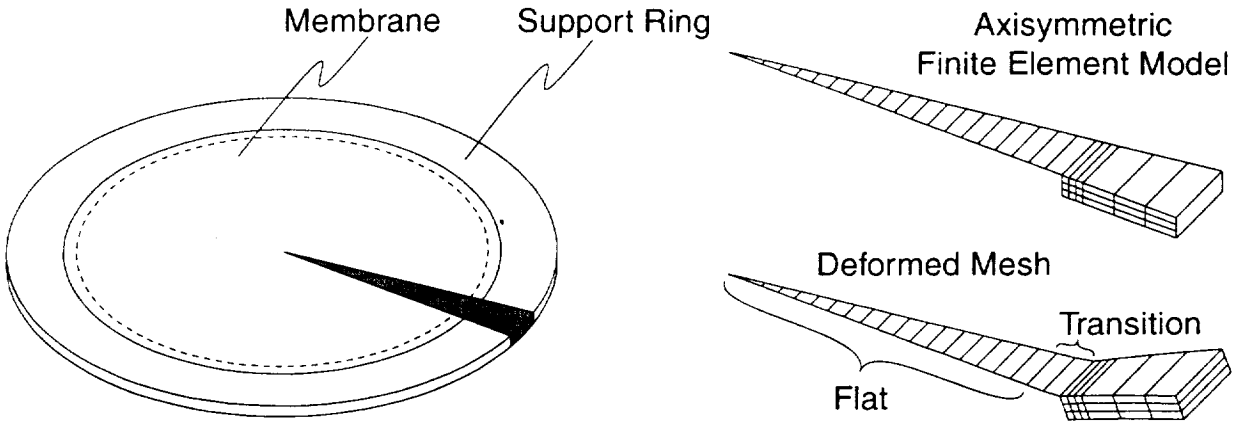

Figure 3. Membrane model consisting of a pre-stressed membrane suspended from a silicon support ring.

3.2. Coating Design[4]

Vacuum deposited thin films exhibit built-in or intrinsic stress, which is characteristic of the material, substrate, and deposition method. This intrinsic stress is due to processes of film formation rather than differential thermal expansion between substrate and film. Thermal expansion generally accounts for lower stress levels, which combine with intrinsic stress to give the total stress in the film.

A common technique for determining coating stress is to measure the deformation of a coated substrate. For the case of an isotropic, homogeneous stress distribution in the coating, and when substrate deformations are small compared to the substrate thickness, the figure of the coated sample is spherical. Coating stress may then be calculated using the following equation from Ref. 5.

$$\sigma = \frac{-\nu_1 H_1^2}{6H_2}\frac{1}{r}\left(1 + 4\frac{\nu_2 H_2}{\nu_1 H_1} - 2\frac{F}{H_1}\right) \tag{1}$$

where the subscripts 1 and 2 refer to the substrate and film, respectively, and

σ =stress, averaged through the film thickness;
H=thickness;
r =radius of curvature of the deformed substrate;
F=center of the film stress distribution normal to the film; $0 < F < H_2$;
$\nu = E/(1-m)$;
E=Young's modulus;
and m=Poisson's ratio.

While physical arguments suggest that the elastic constants of thin films should not differ greatly from those of the same material in bulk, coating stress can depend strongly on details of the coating process. Some film materials exhibit a degree of stress relief upon initial exposure of films to air when the coating chamber is vented. Stress relief can also occur in multi-layer coatings so that the total stress is less than might be expected from summing the stress of layers deposited individually. Achieving quantitative control of stress in a multi-layer design requires experimental measurements for that particular design while properties of the different film materials guide the design process.

The table below gives properties for several useful coating materials gathered from many sources. The notation (?) indicates a probable value where sources differed. Stress values are for individual layers physical vapor deposited on fused silica substrates.

Material	Stress (dyne/cm^2) tensile > 0	Coefficient of expansion (1/K)	Young's Modulus (dyne/cm^2)	Refractive Index
Al_2O_3	4.30E+09	5.60E-06	4.03E+12	1.59
Ge	2.40E+09	5.50E-06	7.50E+11	4.30
MgF_2	3.30E+09	1.37E-06	8.70E+11	1.36
Si	3.70E+09	2.44E-06	9.80E+11	3.60
SiO	8.90E+09	1.50E-06(?)	5.00E+11(?)	1.85
SiO_2	-2.80E+09	5.50E-07	9.00E+11	1.42
ThF_4	9.10E+08	1.40E-05(?)	1.20E+12(?)	1.49
ZnS	-1.60E+09	7.85E-06	8.70E+11	2.25
ZnSe	-9.80E+08	8.10E-06	7.50E+11	2.44

4. MECHANISM

Currently, there is no MEMS mechanism like the one presented herein to the knowledge of the authors. The compatibility of materials and process with the multi-layer dielectric coating together with the size requires the development of unique processes. Development of a closed loop servo controlled electrostatic actuation mechanism to achieve relative parallelism and scanning also represents a unique challenge. In this section we present the simulation results used to design a mechanism for the development and proof of concept of the MEMS FP servo mechanism. Unfortunately, fabrication of this mechanism was not completed at the time of submission. As such the mechanism test results will be presented in future work.

4.1. Electro-Mechanical Static Analysis

The tunable filter design is based on a servo controlled electrostatic actuation mechanism. This mechanism is comprised of three pairs of capacitive pads adjacent to curved spring elements. As a voltage is applied, an attractive force pulls the capacitive pads together. The attractive force is reacted by the force in the spring elements. At some critical voltage, the pads unstably snap together. Theoretical predictions of the electrostatic and mechanical force are given by

$$F_e = \frac{\epsilon V^2 A}{2d^2} \qquad F_m = K_s \delta \tag{2}$$

where ϵ is the permittivity, A is the capacitive area, and d is the gap between electrodes. The term δ is the relative displacement, and the gap $d = d_0 - \delta$ for an initial gap of d_0. An approximation for the curved spring stiffness K_s may be derived for this configuration using Castigliano's theorem,[6] and is given by

$$K_s = \left[\frac{R^3}{4EI}A + \frac{R^3}{4G\kappa}B + \frac{R^2 L}{2G\kappa}C^2\right]^{-1} \tag{3}$$

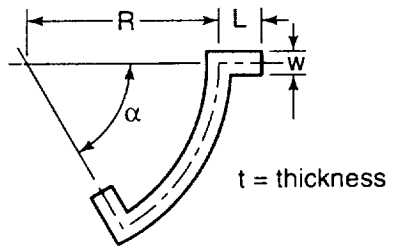

Figure 4. Parameter variation effects on snap-on voltage.

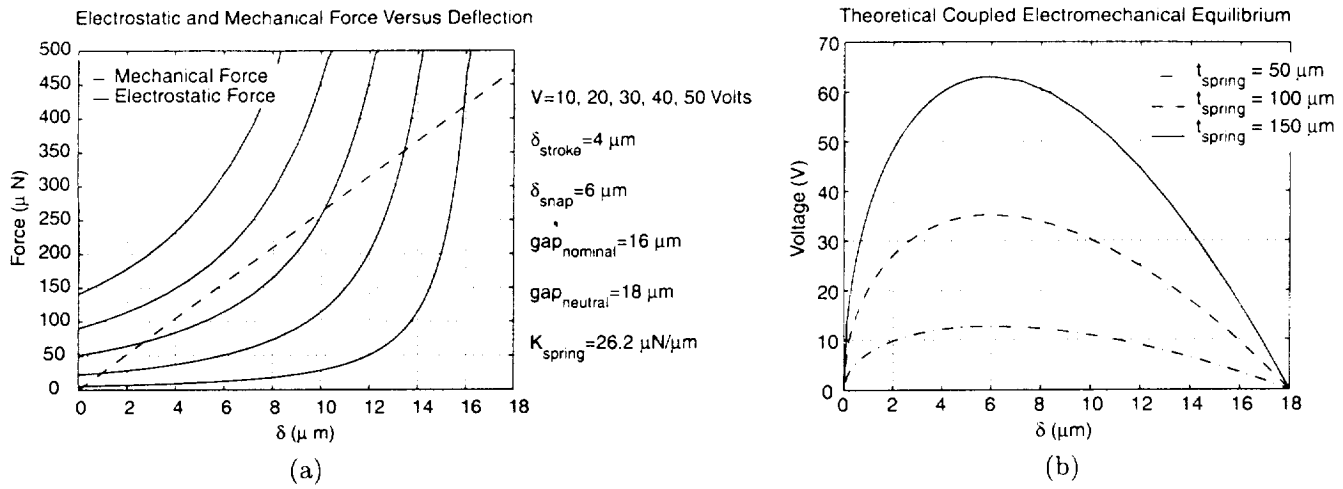

Figure 5. Quasi-static mechanical response of the spring/capacitor system. (a) Electrostatic and mechanical forces. (b) Equilibrium solution for voltage.

where R is the radius of the spring, I is the area moment of inertia, E is the Young's modulus, G is the shear modulus, and the torsional shape parameter κ is given by[6]

$$\kappa = wt^3 \left[3 + 1.462\frac{t}{w} + 2.976\left(\frac{t}{w}\right)^2 - 0.238\left(\frac{t}{w}\right)^3 \right]^{-1}. \tag{4}$$

In the above equation, t is the spring thickness, and w is the spring width. The parameters A, B, and C in equation (3) are given by

$$A = \int_0^{\alpha} \left(2\sin\theta - (1 - \frac{L}{R})\sin\alpha\cos\theta - (1 - \frac{L}{R})(1 - \cos\alpha)\sin\theta \right)^2 d\theta, \tag{5}$$

$$B = \int_0^{\alpha} \left((1 - \frac{L}{R})\sin\alpha\sin\theta - (1 - \frac{L}{R})(1 - \cos\alpha)\cos\theta - 2(1 - \cos\theta) \right)^2 d\theta, \tag{6}$$

$$C = (1 - \frac{L}{R})\sin\alpha \tag{7}$$

where α is the angle swept by the spring and L is the arm length as shown in Fig. 4.

The above expression for the curved spring stiffness was found to be at worst within 15% of finite element simulations. While highly approximate, this expression can be used to conveniently and rapidly conduct parameter sensitivity studies.

Plots of the above equations are shown as a function of displacement in Fig. 5. At equilibrium, the electrostatic and mechanical forces are equal. We can use these equations to solve for the corresponding voltage as a function of the displacement from the initial gap distance.

$$V = \sqrt{\frac{2d^2 K_s \delta}{\epsilon A}} \tag{8}$$

Fig. 5b shows plots of the voltage versus displacement for three different spring thicknesses. When the applied voltage reaches the local maximum on these curves, the actuator will snap-on. By minimizing the corresponding

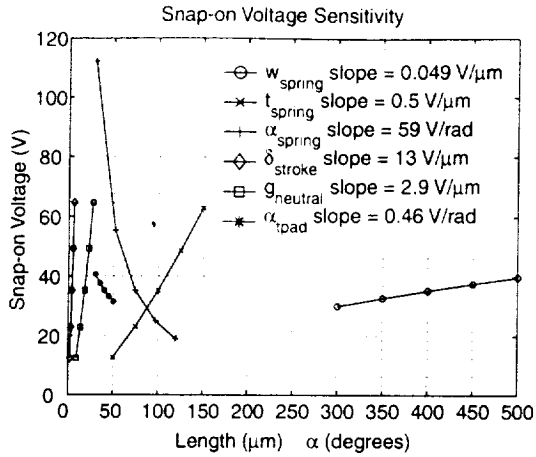

Figure 6. Parameter variation effects on snap-on voltage.

equation, we may show that the snap-on voltage always occurs at a displacement equal to one-third of the initial gap (see Ref. 7). In other words $\delta_{snap} = d0/3$. This may be used to compute the snap-on voltage directly.

$$V_{snap} = \sqrt{\frac{8K_s d_0^3}{27\epsilon A}} \tag{9}$$

This expression is used to study the effects of various design parameters shown in Fig. 6, and is used to size the actuation mechanism components as follows.

Our goal is to maintain full servo control of the mechanism over a range of at least 1 μm with reasonable voltages, without inducing the snap condition. Initially we choose a conservative stroke of 4 μm. The system is highly unstable near the snap-on voltage so we scale the stroke by a factor of 1.5, giving a total theoretical stroke of 6 μm. This requires an initial neutral gap of 18 μm. Note that we may only apply attractive forces electrostatically. As a result, we run the servo from a nominal gap of 16 μm to provide full servo control in both directions.

In addition to the above coating and mechanism analysis, the structure must be designed to survive handling, launch, and space environment loads as well as meet the performance requirement during operation at cryogenic temperatures. In future work, a detailed finite element model of the full device will be developed as needed to predict the dynamic response to launch vibration and acoustic loads and bulk temperature changes from ambient to 30K. The device will also be designed to avoid resonance at the frequencies of the driving servo mechanism.

As electrostatic forces are applied to the actuators, deflections of the springs will induce slight moments on the membrane support ring. These effects will be studied using the integrated model, and the support ring will be dimensioned to react these moments without distorting the optical surface. The effects of gravity during ground based testing will also be accounted for in the design through this detailed analysis. Detailed analysis will be completed as needed to developed flight qualification test plans.

4.2. Electromechanical Frequency Response

Position sensing is base-lined to be be accomplished by measuring the capacitance change in the electrostatic actuator plate spacing. The carrier was chosen to be around 20 kHz which would be well beyond the controller bandwidth. Analysis was done to investigate the position jitter induced by a $+/-$ 10 $volt$ sinusoidal sensor carrier signal and to ensure no resonance would be excited.

Fig. 7 shows a plot of force versus voltage for a single actuator with various actuator gaps. Additionally, the equilibrium curve whereby spring-force equals actuator force is shown. Note that this slope tends toward infinity at the snap-on voltage around 35 $volts$ at a gap of 12 μm.

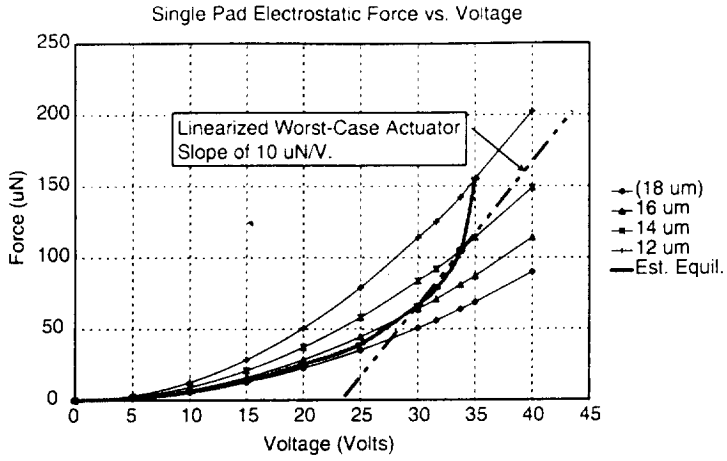

Figure 7. Force versus applied voltage at various gap distances corresponding with Fig. 5.

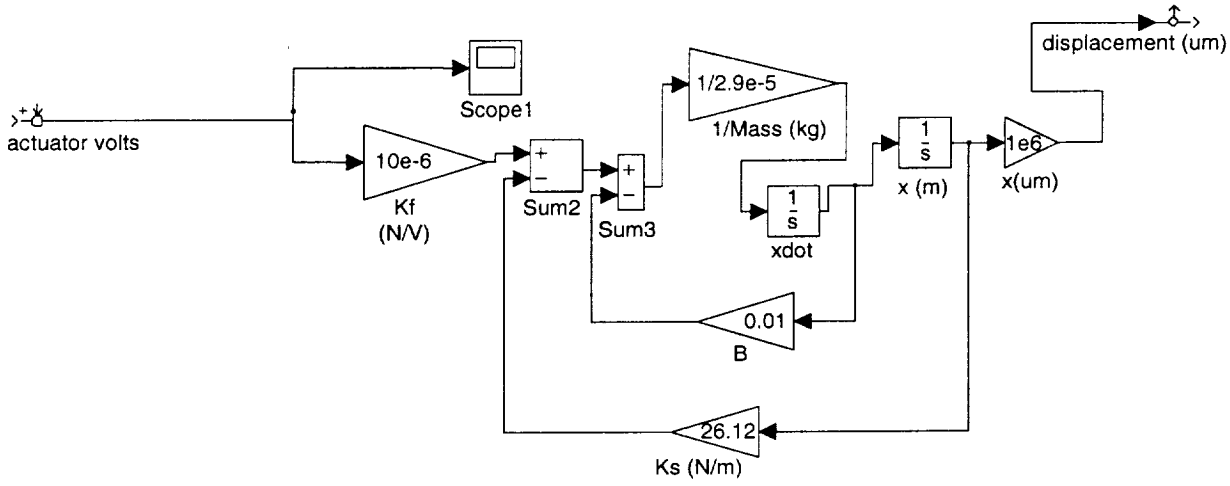

Figure 8. Control system block diagram.

A linear model was generated with Matlab/Simulink[8] and is shown in Fig. 8. Assuming the fundamental mode is one in which all three of the springs move in unison and the optic moves along the optical axis, the behavior can be analyzed using one spring, one actuator and one-third of the suspended mass.

In order to simplify the analysis, a linearized force constant was chosen from the curves in Fig. 7 of 10 $\mu N/V$. The corresponding frequency response is shown in Fig. 9. The system resonance is at 150 Hz which is not a problem for our system. The carrier induces a jitter of 0.4 nm which is acceptable given an overall positioning requirement of 6 nm. It should be noted that although the linearized slope is worst-case there will be a difference in the real system. This linear case, while having a steeper slope, also yields an average force of zero when driven by an AC signal. However, the nonlinear nature of the actuator will give a non-zero average DC force when driven with the carrier signal. This is because more force is produced for voltages above the equilibrium than below since the curve flattens out for lower voltages. This DC bias will vary with position but will be compensated for by the control system.

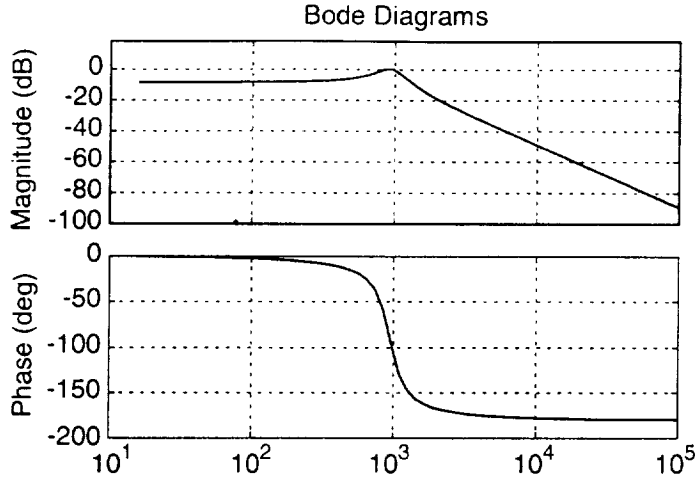

Figure 9. MEMS FP mechanism frequency response diagrams.

5. COMPONENT FABRICATION AND TESTING

In the optical membrane design, we must select a combination of materials that meet the optical requirements, and also provide sufficient intrinsic stress to flatten the membrane under drum-head tension. At the same time the stress must be sufficiently low so as to not induce failure. This design process requires detailed finite element models correlated with experimental results. As a result, witness silicon wafer's were coated along with optical elements from DULCE. The coating materials in that case were a combination of proprietary coating called IRX[9] (with unknown properties), and germanium. The surface profile of the wafer was measured before and after coating and the above equation was used to compute a membrane stress of about $4.4e9\ dyne/cm^2$.

The above film stress data may be used in conjunction with a finite element model of the coated wafer to approximate the elastic modulus of the IRX film. The correlated results may then be used to develop a finite element model of the optical coating suspended as a membrane from a silicon ring. We are currently working on back etching the witness samples to leave a suspended optical coating membrane for flatness measurements. Unfortunately, details of the etching process were not completed at the time of submission of this paper. Results of this test will be forthcoming in future work. These results will be used to correlate a detailed finite element modeling helping to guide the material selection and design of an optical coating that will meet the flatness requirement.

In addition to the above, we are in the process of fabricating the mechanism structure. The etched structures were not available at the time of submission of this paper.

6. CONCLUSION

Detailed modeling and simulation results for a large aperture MOEMS Fabry-Perot tunable filter were presented. In particular, the relatively complicated development task was divided into two sub-components. One is the etalon multi-layer dielectric reflector coatings and the other is the servo mechanism for tunable etalon control.

A large aperture tunable Fabry-Perot interferometer has a stringent reflector flatness requirement. It was shown by analysis, that a membrane with high intrinsic stresses suspended from an annular ring may be designed to meet the requirement. A witness sample with a multi-layer dielectric coating was used to determine the total coating intrinsic stress for one design. These results may be used to build a correlated finite element model and optimize the reflector design.

Analytical static and dynamic coupled electro-mechanical analysis was completed for the servo mechanism, which will be used to control parallelism and gap distance of the etalon. These results were used to size the suspension springs and capacitive actuator pads. While the initial servo mechanism design is completed, fabrication and test results are not currently available.

In future work, the servo mechanism will be tested, and used to develop the computer control system. Subsequently, the multi-layer dielectric coatings will be integrated with the servo mechanism design.

ACKNOWLEDGMENTS

This project was supported by a grant from the NASA/GSFC Director's Discretionary Fund (DDF). The authors gratefully acknowledge Jim Row from Northrop Grumman for providing optical coating design guidance.

REFERENCES

1. Queensgate Instruments Inc, 90 Merrick Avenue, East Meadow, New York 11554, *http://www.queensgate.com.*
2. H. Stockman, *Next Generation Space Telescope, Visiting a Time When Galaxies Were Young*, The Association of Universities for Research in Astronomy, Inc., Washington, DC, 1997.
3. S. Satyapal, M. Greenhouse, R. Barclay, D. Amato, B. Arritt, R. Barry, C. Holt, J. Kuhn, T. Higelman, N. Fonneland, and L. Lesyna, "The tunable filter program for ngst," *Imaging the Universe in Three Dimensions: Astrophysics with Advanced Multi-Wavelength Imaging Devices. ASP Conference Series. AAS Meeting No. 194* , (Chicago, Illinois), May 1999.
4. J. Row. Private communication. Northrop Grumman, Pico Rivera, CA.
5. K. Roll, "Analysis of stress and strain distribution in thin films and substrates," *J. Appl. Phys.* **47**, p. 3224, 1976.
6. J. Shigley and C. Mischke, *Standard Handbook of Machine Design, Second Edition*, McGraw-Hill, New York, 1996.
7. M. Michalicek, D. Sene, and V. Bright, "Advanced modeling of micromirror devices," *Proc. of Int. Conf. on Integrated Micro/Nanotech. for Space Applications* , pp. 214–229, 1995.
8. The Math Works, Inc., Natick, MA, *Matlab Version 5.2*, 1998.
9. CERAC (TM) Incorporated, P.O. Box 1178, Milwaukee, WI 53201, *IRX Optical Coating Material.*